JGR Atmospheres

RESEARCH ARTICLE
10.1029/2024JD041581

Balloon Baseline Stratospheric Aerosol Profiles (B^2SAP)—Perturbations in the Southern Hemisphere, 2019–2022

Elizabeth Asher[1,2], Alexandre Baron[1,3], Pengfei Yu[4], Michael Todt[1,3,5], Penny Smale[6], Ben Liley[6], Richard Querel[6], Tetsu Sakai[7], Isamu Morino[8], Yoshitaka Jin[8], Tomohiro Nagai[7], Osamu Uchino[7], Emrys Hall[2], Patrick Cullis[2], Bryan Johnson[2], and Troy D. Thornberry[3]

[1]Cooperative Institute for Research in Environmental Sciences, University of Colorado Boulder, Boulder, CO, USA, [2]NOAA Global Monitoring Laboratory, Boulder, CO, USA, [3]NOAA Chemical Sciences Laboratory, Boulder, CO, USA, [4]Institute for Environmental and Climate Research Jinan University, Guangzhou, China, [5]Now at Finnish Meteorological Institute, Helsinki, Finland, [6]National Institute of Water and Atmospheric Research, Lauder, New Zealand, [7]Meteorological Research Institute (MRI-JMA), Tsukuba, Japan, [8]National Institute for Environmental Studies (NIES), Tsukuba, Japan

Abstract Volcanic and pyrocumulonimbus (pyroCB) injections into the stratosphere perturb the aerosol layer and can have important radiative and chemical impacts on timescales spanning from months to several years. Repeated in situ balloon-borne measurements of aerosol size and number concentration (>140 nm in diameter), ozone, water vapor, and atmospheric state variables made at midlatitudes in the southern hemisphere (SH) since 2019 enable us to better characterize such events. We use this record and coincident lidar extinction profiles to study several moderate to large stratospheric perturbations in the SH between 2019 and 2022 in detail, including the Australian New Year Super Outbreak (ANYSO) pyroCB in 2020. Median vertical profiles of aerosol number concentration, effective radius, and surface area in SH midlatitudes are also compared with those recorded in Northern Hemisphere midlatitudes under baseline conditions using an identical payload. These data depict the variability in stratospheric aerosol properties in the SH midlatitudes during this period and provide a benchmark for global sectional aerosol models. They reveal that sulfate particle size distributions under baseline conditions and in volcanic plumes are relatively well represented in the Community Earth System Model—Community Aerosol Radiation Model for Atmospheres (CESM-CARMA), but more observations of biomass burning plumes are needed to improve model skill in simulating pyroCB. Comparisons between in situ and lidar observations also highlight a need for more observations of aerosol composition and refractive index in both fresh and aging biomass burning plumes.

Plain Language Summary Particles in the atmosphere scatter incoming sunlight and can influence surface temperatures. When large wildfire and volcanic plumes occasionally reach the upper atmosphere, they can alter the number and size of particles in this region of the atmosphere for months to years. Here, we describe results from repeated balloon-based measurements, ground-based measurements and model simulations of particle number, size, and other optical properties in the Southern Hemisphere between 2019 and 2022 to better understand the impact of such events. We also compare these measurements to similar ones made in the Northern Hemisphere to probe for interhemispheric differences.

Key Points:

- Lower-stratospheric perturbations over SH midlatitudes are linked to Australian New Year's Super Outbreak pyrocumulonimbus and volcanic eruptions
- Median stratospheric aerosol number concentration, surface area and effective radius are similar over SH and NH midlatitudes in 2019–2022
- Balloon particle size distribution measurements indicate work remains to correctly simulate aerosol microphysics in large wildfire plumes

Correspondence to:
E. Asher,
Elizabeth.asher@noaa.gov

Citation:
Asher, E., Baron, A., Yu, P., Todt, M., Smale, P., Liley, B., et al. (2024). Balloon baseline stratospheric aerosol profiles (B^2SAP)—Perturbations in the southern hemisphere, 2019-2022. *Journal of Geophysical Research: Atmospheres*, *129*, e2024JD041581. https://doi.org/10.1029/2024JD041581

Received 16 MAY 2024
Accepted 12 OCT 2024

Author Contributions:
Conceptualization: Elizabeth Asher
Data curation: Elizabeth Asher, Alexandre Baron, Michael Todt, Penny Smale, Ben Liley, Tetsu Sakai, Isamu Morino, Yoshitaka Jin, Tomohiro Nagai, Osamu Uchino, Emrys Hall, Patrick Cullis, Bryan Johnson
Formal analysis: Elizabeth Asher, Alexandre Baron, Pengfei Yu
Funding acquisition: Elizabeth Asher, Tetsu Sakai, Troy D. Thornberry
Investigation: Elizabeth Asher, Pengfei Yu
Methodology: Elizabeth Asher, Michael Todt

1. Introduction

The climate impacts of changes in stratospheric aerosol (i.e., radiative forcing and adjustments) motivate a better understanding of its variability (Kremser et al., 2016; Solomon et al., 2011). Under baseline conditions the stratospheric aerosol layer (Deshler et al., 2003; Junge & Manson, 1961), concentrated between the tropopause and 25 km is primarily composed of sulfuric acid (H_2SO_4) particles formed in situ from sulfur dioxide (SO_2) and carbonyl sulfide (OCS) oxidation as well as mixed organic sulfate particles from the tropical upper troposphere/lowermost stratosphere (UTLS; Froyd et al., 2009; Murphy et al., 2014; Yu et al., 2015; Rollins et al., 2018). Gaps in understanding remain with respect to reoccurring sources of SO_2 that may influence the variable baseline of stratospheric aerosol, despite significant advancements in atmospheric sulfur chemistry (Novak et al., 2021; Rollins et al., 2017, 2018; Veres et al., 2020), the introduction of sectional aerosol models into global climate simulations (e.g., Yu et al., 2015) and better agreement with respect to in situ and space-based measurements (Deshler et al., 2019; Kovilakam & Deshler, 2015). Aerosol nucleation, particle coagulation, gas-phase

Project administration: Richard Querel, Tetsu Sakai, Bryan Johnson, Troy D. Thornberry
Resources: Bryan Johnson, Troy D. Thornberry
Supervision: Richard Querel, Tetsu Sakai, Troy D. Thornberry
Visualization: Elizabeth Asher
Writing – original draft: Elizabeth Asher, Alexandre Baron, Pengfei Yu
Writing – review & editing: Elizabeth Asher

condensation, evaporation, sedimentation, and transport processes shape the aerosol size distributions (Kremser et al., 2016). Large-scale stratospheric transport from the tropics to the poles contributes to the latitudinal spread of aerosols (Andrews et al., 1987) and quasi-biennial oscillation and polar vortex dynamics introduce large scale variability in background stratospheric aerosol (Hitchman et al., 1994). Balloons carrying lightweight instruments can provide detailed information on the aerosol size distribution, which is not directly observable from space, and reach higher altitudes than aircraft. Historically, the majority of regular aerosol sonde measurements have been made at midlatitudes in the northern hemisphere (NH), with episodic measurements at other latitudes.

The stratospheric aerosol layer is also regularly perturbed by volcanic eruptions of varying magnitudes and increasingly by pyrogenic injections (Fromm et al., 2010; Peterson et al., 2021; Schwartz et al., 2020; Solomon et al., 2011; Yu et al., 2019). SO_2 and primary ash aerosol are directly injected into the stratosphere during large explosive volcanic eruptions (e.g., Bègue et al., 2017; Kloss et al., 2021). Large quantities of organic aerosol (Fromm et al., 2010; Peterson et al., 2018) as well as water vapor (H_2O) and other gaseous combustion products (e.g., Khaykin et al., 2020; Pumphrey et al., 2011) can reach the stratosphere during pyrocumulonimbus (pyroCB) events. The climate impacts of volcanic events vary based on the latitude and altitude of injections in addition to their magnitude (e.g., Tilmes et al., 2017). Additionally, differences in the composition of material introduced into the stratosphere, such as a combination of SO_2, ash, and H_2O from volcanoes (Zhu et al., 2020) or smoke particles from pyroCB injections (Yu et al., 2023) influence both the chemistry within the plume and its radiative impacts.

The 2019–2020 Australian bushfires, which began in September 2019 and persisted until February 2020, gave rise to a series of pyroCB in late December and January (hereafter referred to as the Australian New Year's Super Outbreak or ANYSO pyroCB) and has been documented as the most stratospherically impactful wildfire season in the satellite record (e.g., Khaykin et al., 2020). The ANYSO pyroCB led to localized stratospheric warming, smoke induced changes to stratospheric dynamics (e.g., smoke-charged vortices), anomalously high stratospheric H_2O mixing ratios in concentrated plumes, and widespread stratospheric ozone (O_3) depletion (Allen et al., 2020; Damany-Pearce et al., 2022; Kablick et al., 2020; Khaykin et al., 2020; Yu et al., 2021). Analysis of the synoptic scale meteorology and fuel availability necessary to produce pyroCB suggest that their occurrence may be predicted and will become more common (Peterson et al., 2021). Yet, how the pyrogenic injection of biomass burning (BB) aerosol affects climate and chemistry is still not well understood (Burkholder, 2015; Guow and Lovejoy, 1998; IPCC, 2023).

Here, we present balloon-borne measurements of aerosol size distributions in the stratosphere from the southern hemisphere (SH) midlatitudes between 2019 and 2022 obtained through the Baseline Balloon Stratospheric Aerosol Profiles (B^2SAP) project as well as H_2O and O_3. Created to study the global stratosphere under unperturbed conditions as well as following volcanic eruptions, large wildfires, rocket emissions (e.g., Katich et al., 2023), particles from satellite reentry (e.g., Murphy et al., 2023), and potentially future intentional climate intervention activities, the B^2SAP project supports latitudinally distributed aerosol measurements in the NH and SH. We compare our SH midlatitude stratospheric measurements with the corresponding NH midlatitude baseline measurements during this period described in Todt et al. (2023) and discuss a series of perturbations that contributed to a variable stratospheric aerosol layer in the SH. Namely, the midsize volcanic eruption of Ulawun (Kloss et al., 2021) in the summer of 2019, the ANYSO pyroCB in the winter of 2019/2020 (Allen et al., 2020; Kablick et al., 2020; Yu et al., 2021), and the La Soufrière eruption in 2021 (Bruckert et al., 2023) are discussed. Measured aerosol size distributions and those simulated using a sectional aerosol model coupled with a global climate model are compared as well as POPS calculated and lidar-derived extinction profiles. We focus our analysis on isentropes above 380 K. The lowermost stratosphere (i.e., extending from the tropopause to 380 K) and the troposphere are not discussed in detail here due to larger uncertainties in aerosol microphysical properties related to mixed organic sulfate particle composition and potential errors in lidar-derived extinction due to cirrus clouds in this region.

2. Methods

2.1. Launch Site and Payload Description

Small weather balloons (payload weight <2.73 kg) with the Portable Optical Particle Spectrometer (POPS) have been launched periodically (approximately 2–4 times per year) since 2019 from Lauder, New Zealand (45.29°S, 169.67°E, 370 m above sea level, ASL) to measure aerosol size distributions in the UTLS as part of the B^2SAP project. The regular B^2SAP instrument payload consists of a POPS, a NOAA frost point hygrometer (Hall

et al., 2016), an electrochemical concentration cell (ECC) ozone instrument (Komhyr & Harris, 1971), and an iMet radiosonde. Valved balloons limit descent speeds to ∼5 m s^{-1}, enabling sampling of aerosol and water vapor on the descent as well as ascent (limited only by telemetry reception) (Kräuchi et al., 2016). The B^2SAP project at Lauder supplements ongoing monthly soundings of ozone and H_2O started in 2004 at NIWA/Lauder in collaboration with the NOAA global monitoring laboratory (Hurst et al., 2011). In addition, POPS launches from Boulder, CO (39.95°N, 105.20°W, 1,743 m ASL) have taken place through the B^2SAP project regularly since 2019, approximately every two to four weeks with a short sampling gap in 2020 due to the global C.O.V.I.D.-19 pandemic. Launches from Hilo, HI (19.71°N, 155.05°W, 10 m ASL) and from Reunion Island, FR (21.08°S, 55.38°E, 2160 m ASL) began in 2022 at a rate of approximately four per year.

POPS is a high-sensitivity, robust, lightweight, and compact instrument that sizes individual particles within the range of 0.14–2.5 μm (Gao et al., 2013, 2016), assuming particles are composed of sulfuric acid and water under baseline conditions (see below for details). Details regarding the modifications to the original POPS body design and the addition of a variable flowrate that scales with decreasing pressure to improve the instrument's performance at high altitude (low pressure) are described in detail in Todt et al. (2023). By virtue of their size and number, accumulation mode stratospheric aerosol is the most efficient at scattering light back out to space and cooling the earth (Murphy et al., 2021). POPS measurements can quantify at least nine tenths of aerosol radiative effects (and net cooling) with unit efficiency (Gao et al., 2016; Murphy et al., 2021).

2.2. Data Telemetry and Processing

For launches between 2019 and 2022 from Lauder, where the payload is rarely retrieved (not the case for NH midlatitude measurements—see Todt et al., 2023 for details), particles were sorted based on their diameter into 15 size bins (a maximum dictated by the radiosonde data bandwidth). The bin edges are lognormally distributed in POPS signal space on all flights prior to 2020-06-19 and lognormally distributed in Dp space thereafter (see supporting data for details). Telemetered POPS data were arithmetically averaged within 0.1 km altitude on ascending and descending vertical profiles and merged with corresponding arithmetically averaged radiosonde air pressure, corrected air temperature, quality assured NOAA FPH H_2O and ECC ozone mixing ratios. Unless otherwise noted, mean ascending and descending vertical profiles of aerosol properties and water vapor are shown here. Radiosonde data are used to calculate the lapse rate tropopause on ascent. In the event of a double tropopause, the second tropopause was used as the transition to the stratosphere. POPS data are quality assured based on flow and instrument noise engineering parameters to yield aerosol size distributions (dN/dlogDp), total number concentration, effective radius ($r_e = m^3/m^2$), total dry aerosol surface area density, and dry volume. Total ambient surface area and extinction were calculated using ambient particle diameters, as described below.

2.3. Ambient Aerosol Size and Aerosol Extinction

Aerosol extinction at 532 nm was calculated based on Mie scattering formulas (Bohren & Huffman, 1983) using the PyMieScatt python package (Sumlin et al., 2018) for comparison with lidar measurements. Like other optical particle sizing instruments, POPS particle sizing requires assuming a spherical particle shape and an index of refraction (IR) specific to its laser wavelength (405 nm). Air masses likely linked to the ANYSO pyroCB were assigned a "smoky" bulk IR, estimated based on the self-lofting altitudes of particles (P. Yu et al., 2021). Simulations suggested that these particles were composed of 2.5% BC and 98% organic material. Due to transit times ≥60 hours and the short lifetime of brown carbon (e.g., Forrister et al., 2015), its contribution to the IR was not explicitly considered. The IR of organic aerosol was assumed to be 1.53 + 0j (Aldhaif et al., 2018), and the IR of BC was assumed to be 1.75 + 0.73j (Kirchstetter et al., 2004; Shamjad et al., 2012), resulting in a bulk IR for internally mixed "smoky" aerosol of 1.54 + 0.018j (Table 1). This is similar to values used by Ohneiser et al. (2022) for smoke aerosols (1.48 ± 0.1 + 0.02j) from the ANYSO pyroCB. For all other air masses, we assumed a bulk IR of 1.45 + 0j (Table 1). This IR is similar to that of (dry) sulfate for stratospheric aerosol because as described in Asher et al. (2023), particles are expected to be at equilibrium with the POPS instrument temperature at the time of detection, which is typically 50–75°C higher than stratospheric air temperatures.

More in situ measurements of aerosol chemical composition in the fresh and aged BB plumes (e.g., Katich et al., 2023) would aid in constraining stratospheric aerosol optical properties and climate impacts. The range of calculated mean bin sizes for smoke (with two alternative smoke IRs) and sulfate particles is shown in Figure 1a. Particle sizing and calculated extinction is sensitive to the choice of IR and the limited number of size bins

Table 1
Assumed Bulk IR for POPS Particle Size Distribution Measurements on Launches From SH Midlatitudes Between 2019 and 2022

Launch date	Altitude	Assumed IR	Extinction uncertainty
2019-04-30	to 24.2 km	1.45 + 0.0j	67%
2019-09-03	to 28 km	1.45 + 0.0j	55%
2020-01-27	to 15.5 km	1.45 + 0.0j	41%
2020-01-27	15.5–17.5 km	1.54 + 0.018j	41%
2020-01-27	17.5–27.6 km	1.45 + 0.0j	41%
2020-06-19	to 27.7 km	1.54 + 0.018j	67%
2020-07-23	to 24.4 km	1.54 + 0.018j	41%
2020-11-17	to 28.1 km	1.45 + 0.0j	62%
2021-08-31	to 26.6 km	1.45 + 0.0j	49%
2021-11-03	to 27.5 km	1.45 + 0.0j	66%
2022-01-24	to 21.1 km	1.45 + 0.0j	81%

Note. Altitude and extinction uncertainty of each POPS profile are also provided. If not stated, the minimum altitude for inferred IR is 10 km.

(yielding a relatively sparse size distribution). In the absence of increasing the number of size bins, calculating a weighted mean bin diameter using the number concentration in the previous and current bin as weights (an arithmetic mean bin size is used in the first bin, and whenever a weighted average cannot be calculated) is used to minimize errors related to the limited number of bins. As an example, we show the uncertainty in aerosol surface area and extinction from 07 to 23–2020 (Figures 1b and 1c), when an abundance of larger size particles was observed following the ANYSO pyroCB (see below for details). Uncertainty in calculated extinction for each profile is listed in Table 1.

Ambient sizes of stratospheric sulfate (H_2SO_4) particles were calculated based on Steele and Hamill (1981) as in Asher et al. (2023) from the measured particle diameter, the particle weight percent and particle density using the partial pressure of H_2O calculated with NOAA FPH measurements and radiosonde air temperature (Gmitro & Vermeulen, 1964; Oca et al., 2018; Tabazadeh et al., 1997; Washburn, 1928). Ambient particle sizes of organic aerosol following the ANYSO pyroCB were calculated based on kappa-Koehler theory (Petters & Kreidenweis, 2007). Low H_2O mixing ratios (ranging from 3–6 ppmv; 0.1%–4% RH) and air temperatures (ranging from −65 to −45°C), resulted in small corrections to the measured diameter under ambient conditions in the stratosphere. Changes to the real IR (<0.005) based on internal mixtures of water and H_2SO_4 in the stratosphere are ignored.

2.4. CESM-CARMA

The Community Earth System Model Community Aerosol Radiation Model for Atmospheres (CESM-CARMA) represents particles composed of internal mixtures of sulfate, organics, black carbon, sea salt, and dust with 20 size bins (0.1–17 μm diameter), operating within CESM1 (Yu et al., 2015, 2021). IR in the CARMA model is wavelength dependent, but in the mid-visible range this equates to IR = 1.95 + 0.79i for BC, 1.4 + 0.0i for OM, and 1.43 + 0.0i for sulfate particles. CESM1's 56 vertical levels extend from the surface to 45 km, yielding a vertical resolution of ∼1 km in the troposphere and lower stratosphere, which increases gradually with altitude to ∼1.5 km in the upper stratosphere, at a horizontal resolution of 1.9° latitude by 2.5° longitude. Aerosol optical properties are calculated using the Multiple Scattering T-Matrix Method (Mackowski and Mischenko, 2011). This simulation includes emissions from volcanic eruptions between 2019 and 2022 (e.g., Ulawun in June and August 2019, Taal in January 2020, Krakatau in April 2020, and La Soufrière in April 2021) as well as from the ANYSO pyroCB. The volcanic and wildfire emissions are listed in Table S1 in Yu et al. (2023). The model temperature and winds are nudged to the Goddard Earth Observing System-5 (GEOS-5) except for a 2-month period following the ANYSO pyroCB, to simulate self-lofting-BB plumes. We use ∼10-day averaged model output of geopotential height, potential temperature, total number concentration, and extinction for comparison with POPS and lidar measurements.

2.5. Lidar Extinction Profiles

Lidar measurements at NIWA in Lauder, NZ began in 1992 (Sakai et al., 2016). We used aerosol extinction profiles retrieved from lidar backscattering measurements at 532 nm between April 2019 and January 2022, concurrent with B^2SAP launches. A detailed description of the lidar and the inversion method can be found in Sakai et al. (2016).

The extinction-to-backscatter ratio (i.e., the lidar ratio), used to invert the lidar profiles is 46 ± 15 sr for sulfuric acid particles during unperturbed periods (Sakai et al., 2016). For six of the nine vertical profiles in this study, we use this value. In the fresh BB plume (observed between 15.75–17.5 km altitude on 27 Jan. 2020) and for two stratospheric profiles within the first seven months of 2020 after the ANYSO pyroCB (June and July 2020), we use the mean lidar ratio (LR) reported above Punta Arenas, Chile by Ohneiser et al. (2020) for the same plume (97 ± 15 sr). A variable (and decreasing) extinction-to-backscatter ratio in the months following the ANYSO pyroCB (Ohneiser et al., 2022) suggests evolving particle composition within the aging biomass burning plume.

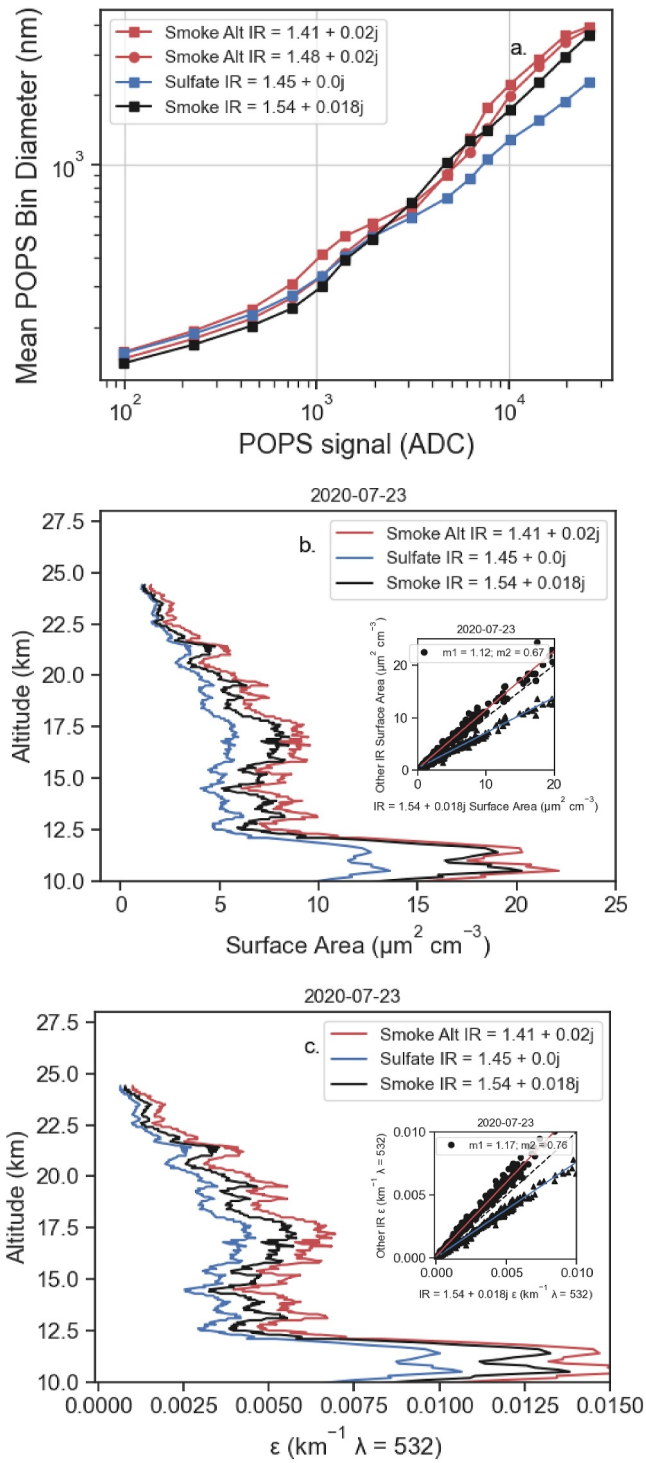

Figure 1. POPS signal versus the calculated mean bin diameter, assuming two different aerosol compositions (smoke and sulfate) and multiple IRs: assumed smoke IR = 1.54 + 0.018j as described in Methods Section 2.3, the alternative smoke IRs = 1.41 + 0.02j and 1.48 + 0.02j and sulfate IR = 1.45 + 0.0j (a). Resulting differences in total particle surface area (b) and extinction (c) based on the range of different assumptions of particle composition and IR (1.48 + 0.02j is omitted here for clarity as it falls within the range shown), for one profile from 2020 to 07–23. Inserts show the simple linear regression between IR = 1.54 + 0.018j and IR = 1.41 + 0.02j (red line) and between IR = 1.54 + 0.018j and IR = 1.45 + 0.0j (blue line) surface area (a) and extinction (b), relative to the 1:1 line (black dashed line). The slopes of the linear regressions are printed in the legend. The uncertainty in the POPS calculated extinction is the difference between these two slopes (e.g., 41%), calculated individually for each profile and shown in Table 1.

Due to lack of available data on particle composition within the ANYSO plume, however, a single bulk IR is assumed here for all "smoky" particles to calculate extinction.

The lidar data set screens for clouds by eliminating raw signals below 0.005 MHz of the photon count rate below 30 km. This method may be susceptible to artifacts from thin cirrus, which are difficult to screen out. As a result, comparisons between POPS and lidar data exclude the upper troposphere.

3. Results and Discussion

3.1. Balloon Observations of Aerosol, Ozone, and Water Vapor in the SH Midlatitudes, 2019–2022

Periodic soundings from Lauder, NZ bound the variability in aerosol properties, H_2O, and ozone with altitude between 2019 and 2022 (Figure 2). For reference, median SH concentrations (bold black line) are shown alongside those from Boulder Colorado (39.9°N, 105.2°W) under baseline conditions during this period (bold red line). Several perturbed profiles discussed below, for instance, from 2019 to 09-03 following the Ulawun volcanic eruption (red line), from 2020 to 01–27 (dark red line) and from 2020 to 07–23 (tan line) following the ANYSO pyroCB with fresh and aged biomass burning influence are shown in color, as opposed to in gray.

Figures 2a–2d show aerosol properties of 9 periodic POPS soundings in the SH between 2019 and 2022. Median particle number concentration in ambient air decreases with ascending altitude at a similar rate above 17.5 km in the SH (mean $\pm 1\sigma$; 0.55 ± 0.18 cm^{-3} km^{-1}) and in the NH (0.64 ± 0.10 cm^{-3} km^{-1}; Figure 2a). Between 12–17.5 km (in the UTLS), the decrease in particle number concentration with altitude differ somewhat in the SH midlatitudes (1.35 ± 0.53 cm^{-3} km^{-1}) and in the NH midlatitudes under baseline conditions (0.66 ± 0.33 cm^{-3} km^{-1}). Few stratospheric sources of aerosol exist in midlatitudes, compared with the tropics, where particle nucleation in the UTLS occurs regularly (e.g., Williamson et al., 2019), and fresh volcanic plumes and pyroCB clouds were not observed above 17.5 km. As a result, the aerosol mixing ratio, 62 ± 1.2 cm^{-3} at standard temperature and pressure (S.T.P.; 0°C and 1 atm) is conserved above 17.5 km and was slightly elevated between 13–17.5 km over SH midlatitudes (71 ± 1.0 cm^{-3} S.T.P.; Figure 2b). Surface area mixing ratios varied little in the SH (13 ± 2.6 μm cm^{-3} S.T.P.) between 15 and 25 km altitude, similar to in the NH under baseline conditions during this period (15 ± 2.6 μm cm^{-3} S.T.P.; Figure 2d). Increases in aerosol surface area have implications for (faster) heterogenous chemistry in the stratosphere. The median aerosol effective radius peaked at ~185 nm in both the NH and SH midlatitudes (Figure 2c). This maximum in particle size occurred at 19 km in the Junge layer.

Figures 2e and 2f show 33 regular O_3 and H_2O soundings in the SH between 2019 and 2022. Between 2019 and 2022, median H_2O mixing ratios reach a minimum in the UTLS in the SH (3.6 ± 0.1 ppmv) and gradually increase with altitude in the stratosphere (to 5.2 ± 0.1 ppmv at 27 km). Median H_2O profiles in the NH and SH appear very similar above 18 km, ranging from approximately 4.2 ± 0.1 ppmv at 18 km to 5.2 ± 0.1 ppmv at 27 km (Figure 2b). Stratospheric O_3 is also similar in NH and SH midlatitudes, ranging from approximately 1 ± 0.3 ppmv at 18 km to approximately 6.3 ± 0.3 ppmv at 27 km (Figure 2e). In the SH, the UTLS has slightly lower H_2O and slightly higher O_3 than in the NH, primarily driven by differences in tropopause heights between the two locations, shown in Figure 2 (interhemispheric UTLS differences are not apparent when plotted in tropopause relative coordinates).

Vertical profiles from 27 January 2020 show that this suite of instruments can be used to identify biomass burning air masses in the stratosphere as well as fresh volcanic plumes (e.g., Todt et al., 2023). The ANYSO, occurring between December 29 and January 4 date, generated 18 pyrogenic injections (Kablick et al., 2020), resulting in ~900 kt of smoke (Yu et al., 2021) and localized H_2O anomalies >15 ppmv (Allen et al., 2020; Schwartz et al., 2020). Although we did not observe anomalies in air temperature or ozone on 27 January 2020 (Figure 3a), expected in the densest smoke plumes emanating from the Australian wildfires (e.g., Kablick et al., 2020), Figure 3b shows a stratospheric airmass influenced by BB. Between 15.5 and 17.75 km altitude (82–117 hPa), we observed corresponding enhancements in H_2O of ~2 ppmv and in total aerosol volume of 5.9 μm^{-3} cm^{-3} with altitude. These enhancements represent a ~100% increase in H_2O and ~5,000% increase in aerosol volume, respectively, compared to the median values between 2019 and 2022 over the SH midlatitudes. NOAA Hysplit back trajectories track the air mass' location 60 hr earlier to 16–18.5 km altitude over the Australian continent, where extensive bush fires persisted (Figures 3c–3e). Air masses above and below these enhancements originated from altitudes between 15.5–19 km over the Tasman Sea and Southern Ocean, respectively. A subsequent O_3 and H_2O sounding on 11 January 2021 from Lauder shows a substantial positive water vapor anomaly of >2 ppmv and

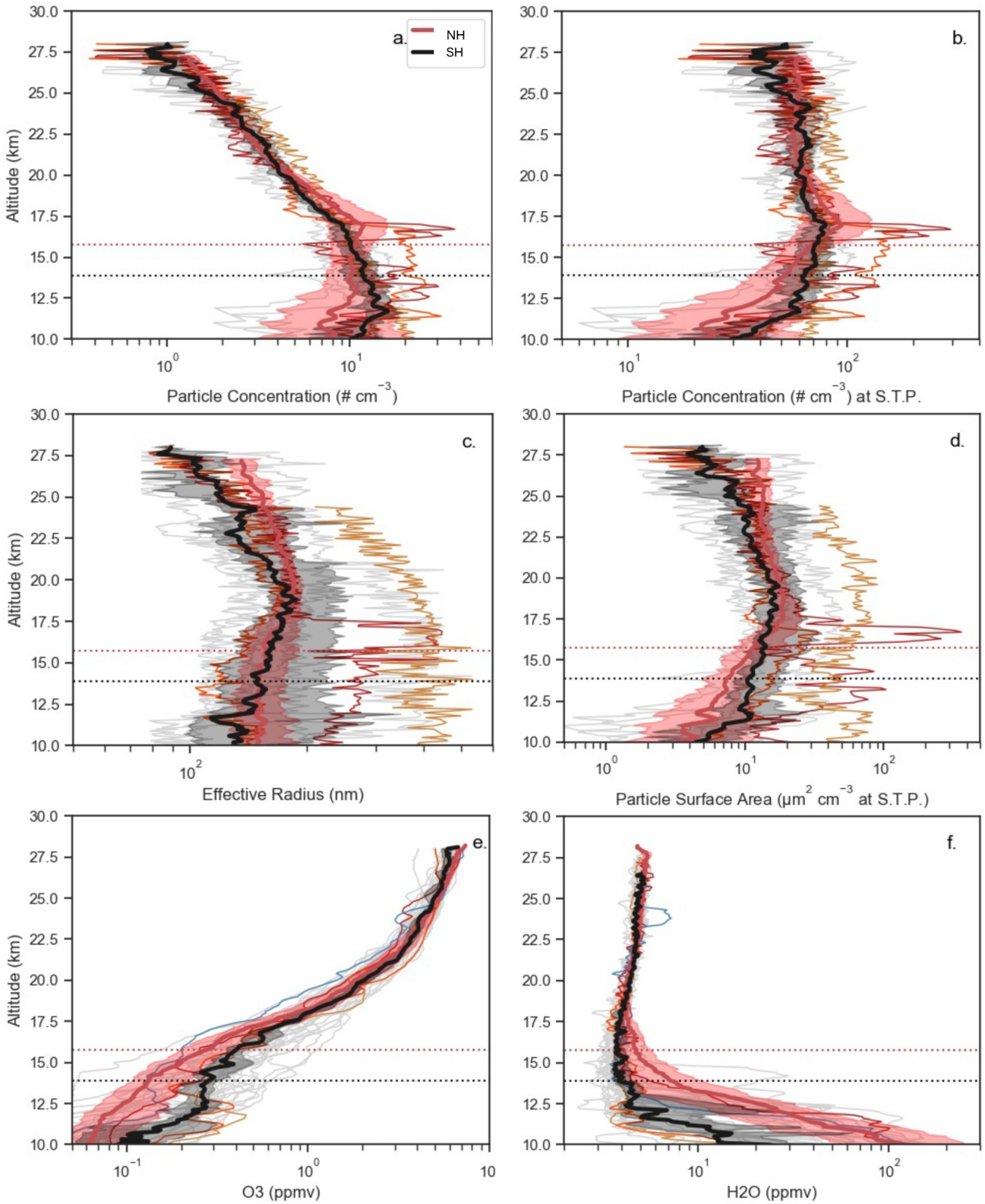
a.
NH
SH
b.
c.
d.
e.
f.
Altitude (km)
Particle Concentration (# cm^{-3})
Particle Concentration (# cm^{-3}) at S.T.P.
Effective Radius (nm)
Particle Surface Area (μm^2 cm^{-3} at S.T.P.)
O3 (ppmv)
H2O (ppmv)

Figure 2.

negative ozone anomaly of >1 ppmv between 23 and 25 km (Figures 2e and 2f; blue dashed line) well outside of the natural variability observed in the stratosphere. We suspect that these O_3 and H_2O anomalies are lingering impacts from the ANYSO pyroCB. Lidar profiles from Punta Arenas indicate aerosol extinction remained elevated between 20 and 25 km through June 2021, and ozonesonde profiles from Neumayer Station, Antarctica (70.67 S, 8.27 W) as well as Lauder, NZ show corresponding negative ozone anomalies at these altitudes (Ohneiser et al., 2022). To the best of our knowledge, the soundings discussed represent the only in situ observations of stratospheric aerosol size distributions and H_2O anomalies within the ANYSO pyroCB plume. Other observed stratospheric perturbations in particle number concentration or volume between 2019 and 2022 did not occur simultaneously with water vapor enhancements.

3.2. Observed and Simulated Aerosol Microphysical Properties

In situ size distribution measurements provide detailed information on evolving SH stratospheric aerosol microphysical properties (Figure 4). A vertical profile on 2019-04-30 shows an unperturbed stratospheric aerosol layer over SH midlatitudes, with moderately high concentrations of particles ≤400 nm diameter between 16–18 km altitudes. On 2019–09–03, we observed an enhancement in particle number (≤400 nm in diameter) as high as 16.5 km (Figure 4b; Figure 2, red line). Enhancements in particle number of small and moderate size particles resulted in a small increase in the total surface area and had no effect on the aerosol effective radius. Remote sensing measurements indicate a modest enhancement in stratospheric aerosol optical depth (sAOD) centered at 40°S between September and November (Kloss et al., 2021). The corresponding increase in H_2SO_4 aerosol mass (e.g., 4–5 × 10–14 g cm^{-3} to 9 × 10–14–1.1 × 10–13 g cm^{-3} between 15.5–16.75 km or 1.92 × 10–8 g cm^{-2} in the lower stratosphere) would require a 36–91 pptv source of SO_2 or 1.25 × 10–7 SO_2 g km^{-2}, equal to 0.5 kt SO_2 homogenously distributed over a 2,000 km × 2,000 km square area. Although baseline values of SO_2 in the UTLS are between 3 and 5 pptv (Rollins et al., 2017, 2018), two eruptions from the Ulawun volcano (5.05°S, 151.33°E), on June 26th and 3rd August 2019 (maximum volcanic explosivity index 4) together released between 350–450 kt SO_2 and its plumes were observed as high as 19 km, dispersing and drifting poleward (Global Volcanism Program, 2019). SO_2 has a typical stratospheric lifetime of ∼1 month, and on 26 July 2019, excesses of 0.5 kt SO_2 remained visible over the northern island of New Zealand (Global Volcanism Program, 2019). Relatively few small particles (<400 nm) were observed in the stratosphere after the ANYSO pyroCB (Figures 4c–4e). Our measurements show the BB plume rose to an altitude 24 km from 17.5 km on 27 January 2020, in agreement with previous studies (Allen et al., 2020; Kablick et al., 2020; Yu et al., 2021). In aged BB airmass sampled on 2020-07-23 (and 2020–06–19), we observed bimodal aerosol size distributions in the stratosphere between 15 and 20 km (410–480 K), which would be imperceptible from remote sensing measurements (Figures 4d–4e). We note that bimodal aerosol size distributions were not observed after any of the volcanic eruptions during this period in either the SH or NH (Todt et al., 2023). By 2020–11–17, the stratosphere appeared to relax toward an unperturbed state. On this vertical profile, we observed no large particles (>600 nm diameter) but elevated concentrations of moderate size particles (400–600 nm diameter) and an increase of small particles (<300 nm in diameter) between 15 and 19 km (Figure 4f). Although it is difficult to identify a single likely source of sulfate or other aerosol responsible for this observed increase in number concentration, lesser volcanic eruptions, such as Taal (14°N, 120°E on January 2020) and Krakatau (6°S 105°E in April 2021) could have contributed to stratospheric aerosol, particularly if paired with overshooting convection (Distributed by Smithsonian Institution, compiled by Venzke, E., 2023), occurring most often (though still not often) in the tropics (e.g., Rollins et al., 2017).

We focus our analysis with respect to model–measurement size distribution comparisons on two isentropes, 400 K–420 K (in the lower stratosphere) and 500–520 K (in the lower-middle stratosphere) between 3 September 2019, following the Ulawun eruption, and 17 November 2020, nearly one year after the ANYSO pyroCB (Figure 5). CESM-CARMA aptly simulates the shape of the size distributions in the volcanic plume case (Figure 5a), after an injection of SO_2 from the Ulawun eruption, in the unperturbed, above plume cases

Figure 2. Vertical profiles of total aerosol number concentration (>140 nm) (a), number concentration at S.T.P. (b), aerosol effective radius (c), aerosol surface area at S.T.P. (d), water vapor (e) and ozone (f) with altitude between 2019 and 2022 over Lauder, NZ (45°S). Black bold lines and shaded regions show the median profiles ± the inner quartile range (IQR) of profiles over Lauder. Red bold lines and shaded regions show the median profiles ± IQR of baseline profiles (Todt et al., 2023) over Boulder, USA (40°N). Individual profiles over Boulder are not shown. Perturbed SH profiles on Sept. 9, 2019 (red line), 27 Jan. 2020 (dark red line), 23 July 2020 (tan line), and 11 Jan. 2021 (blue line). Other SH profiles shown in gray. Dotted horizontal lines indicate the mean lapse rate tropopause height in the SH (black) and NH (red).

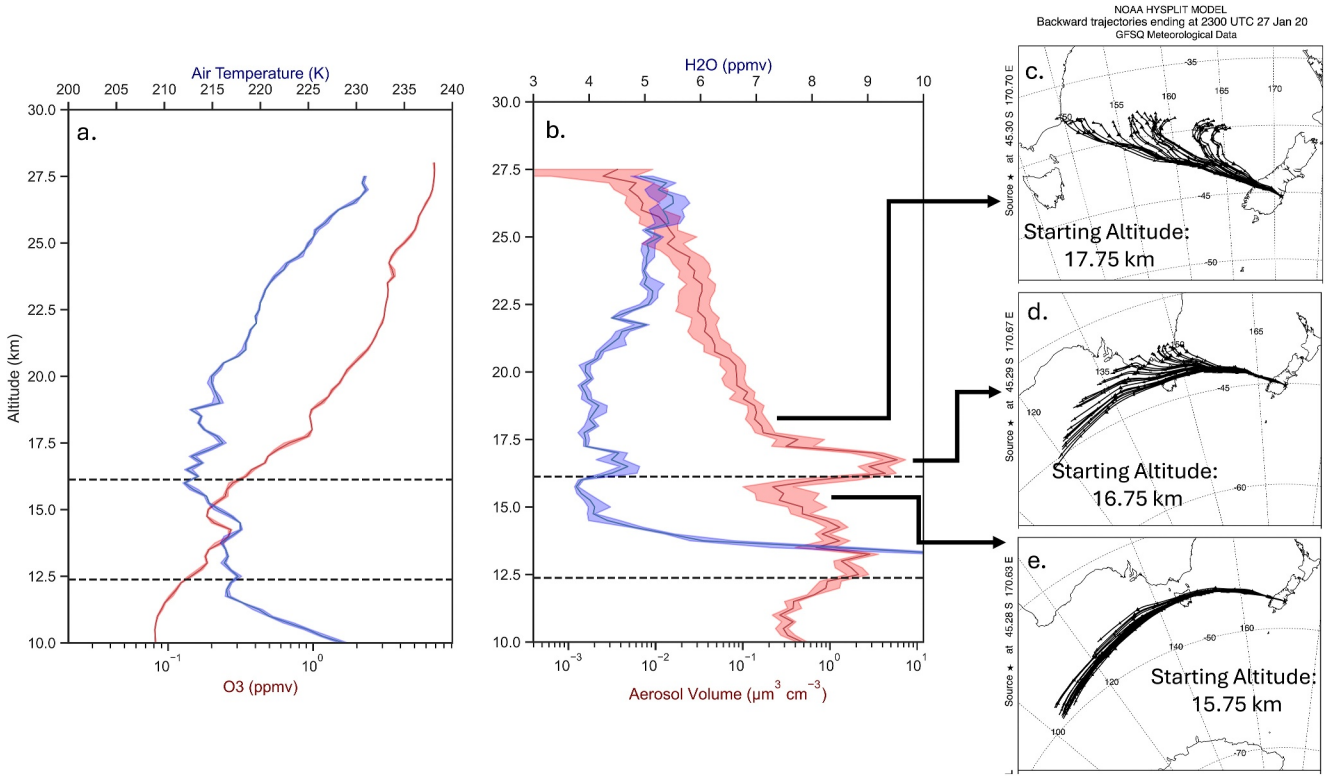

Figure 3. Ascending vertical profiles of air temperature and ozone (a), water vapor and total aerosol volume (>140 nm; b), and NOAA HYSPLIT ensemble 60 hr back-trajectories from 27 January 2020 using hourly 0.5° GFS winds to identify air masses likely influenced by the Australian PyroCB (c–e). The double tropopause is shown as dashed black lines.

(Figures 5b and 5d), and in the approaching baseline cases (Figures 5g and 5h). In the volcanic plume case, both the observations and the model show an increase of small particles ≤300 nm in diameter in the lower stratosphere, although the simulated number concentration is lower (by a factor of ∼2) than the observed number concentration in size bins ≤300 nm in diameter (a smaller difference between the model and measurements is observed in the above volcanic plume and approaching baseline cases). Sampling biases in a fresh biomass burning plume may be expected to contribute to the disagreement shown in Figure 5c. Yet CESM-CARMA also struggles to reproduce the observed bimodal size distributions between ∼100 nm and 2 μm in diameter extending from the lower to the middle stratosphere for the aged biomass burning cases (Figures 5e and 5f; Figure 4d). In these cases, the model underestimates the number concentration of large particles (>500–700 nm in diameter) by more than a factor of two and as much as two orders of magnitude (Figure 5c). Although the sensitivity in POPS aerosol sizing to IR (e.g., Figure 1) may contribute to these model-measurement differences, using an alternative smoke IR does little to alter the bimodal shape of the particle size distribution. Two observed mode diameters occur between 400 and 500 nm and between 1 and 1.4 μm, which are not simulated by the model. CESM-CARMA would suggest instead that the highest number concentration occurred at the smallest sizes. Interestingly, CESM-CARMA has successfully simulated bimodal aerosol distributions after a large volcanic eruption (e.g., Li et al., 2024). The discrepancy between the simulated and observed size distributions in the aged biomass burning cases in particular highlights a need for further model development with respect to pyroCB clouds.

3.3. In Situ Lidar Aerosol Optical Properties

Ambient extinction at 532 nm, calculated from in situ size distribution measurements, is compared with lidar-derived vertical profiles of aerosol extinction (Figure 6). The average correlation for these 9 pairs of POPS and lidar profiles is greater than $r^2 = 0.75$ above 11 km and up to 27 km (Figure 6k). Lidar observations often fall within the POPS uncertainty (the bulk IR assumption for POPS sizing and size-distribution conversion to extinction translates into large uncertainties for POPS-derived extinction). The smoke-influenced layer on 27 January 2020 was observed at slightly different altitudes according to POPS and lidar measurements (Figure 6c).

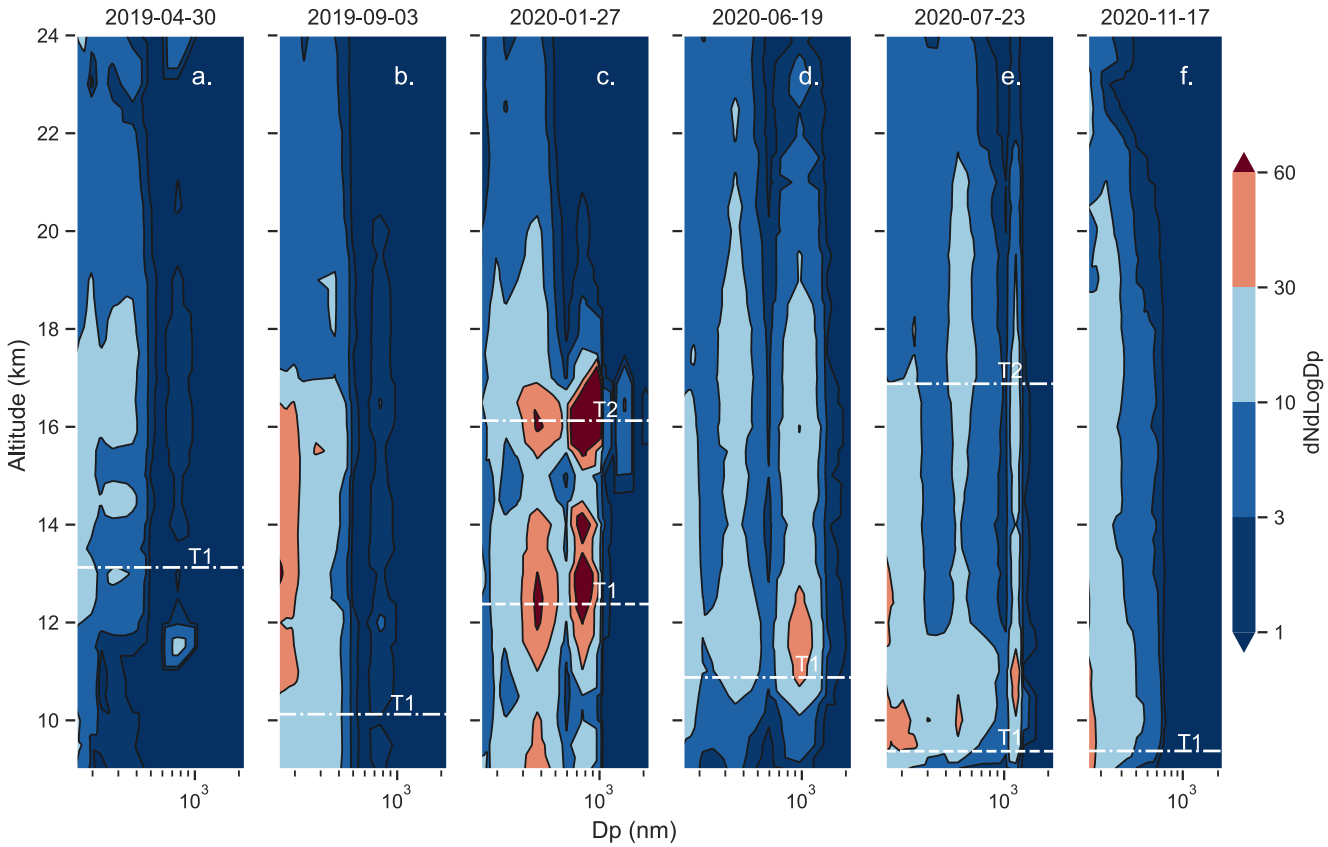

Figure 4. Mean ascending and descending measured aerosol size distributions with altitude on six soundings (a–f) between 30 April 2019 (a) and 17 November 2020 (f). A sulfate IR = 1.45 + 0j was assumed, except for air masses likely influenced by BB when an IR = 1.54 + 0.018j was assumed (see Table 1 for details). The lapse rate tropopause, labeled T1, or double tropopause, labeled T1 and T2, are shown for each vertical profile.

This leads to a notch in the correlation profile just below 16 km. The mean bias shows that the two data sets are on average within ±50% from each other (Figure 6k), indicating an absence of systematic bias over the range of assumed aerosol compositions and IRs. The root-mean-square error (RMSE) is at its highest below 18 km, likely driven by the strongest discrepancies in profiles c, e, g, and i of Figure 6. These differences in RMSE can be attributed to (a) an imperfect temporal overlap, (b) the uncertainty in the LR used to derive aerosol extinction, and (c) the uncertainty in the POPS calculated extinction given a sparse size distribution. Additionally, the aerosol layer is often more perturbed with decreasing altitude in the stratosphere, leading to evolving aerosol distributions on short timescales and poor agreement, even within a day. Above 18 km, differences remain, in particular for the smoke-influenced profiles (c, d, and e) but also other cases (g, h and, i). Furthermore, variable levels of depolarization within the plume (Ohneiser et al., 2022), particularly within the first month after the ANYSO pyroCB, suggests that irregularly shaped fresh biomass burning particles could also have contributed additional unknown errors in calculated extinction based on the aerosol size distribution. For the sulfate-only cases (a, b, f, g, h, and i) the LR of 46 ± 15 sr may be slightly underestimated considering recent results of LR measurements after small eruptions (Prata et al., 2017). Overall, this comparison of independent data sets reveals reasonable agreement despite some significant discrepancies likely due to the need to better constrain the IR and LR, and ultimately calls for more aerosol composition measurements in the stratosphere. Finally, the stratosphere is also characterized by low values of extinction and aerosol concentration, especially outside of perturbated periods, leading to an increased sensitivity to imprecise assumption for indirect retrievals.

3.4. Evaluating State of the Art Climate Models Using a Combination of Observations of Aerosol Optical Properties and Microphysical Properties

Simulated bulk aerosol properties from global climate models are often validated against balloon-based and ground-based measurements. Figure 7 compares simulated CESM-CARMA particle number concentration in the

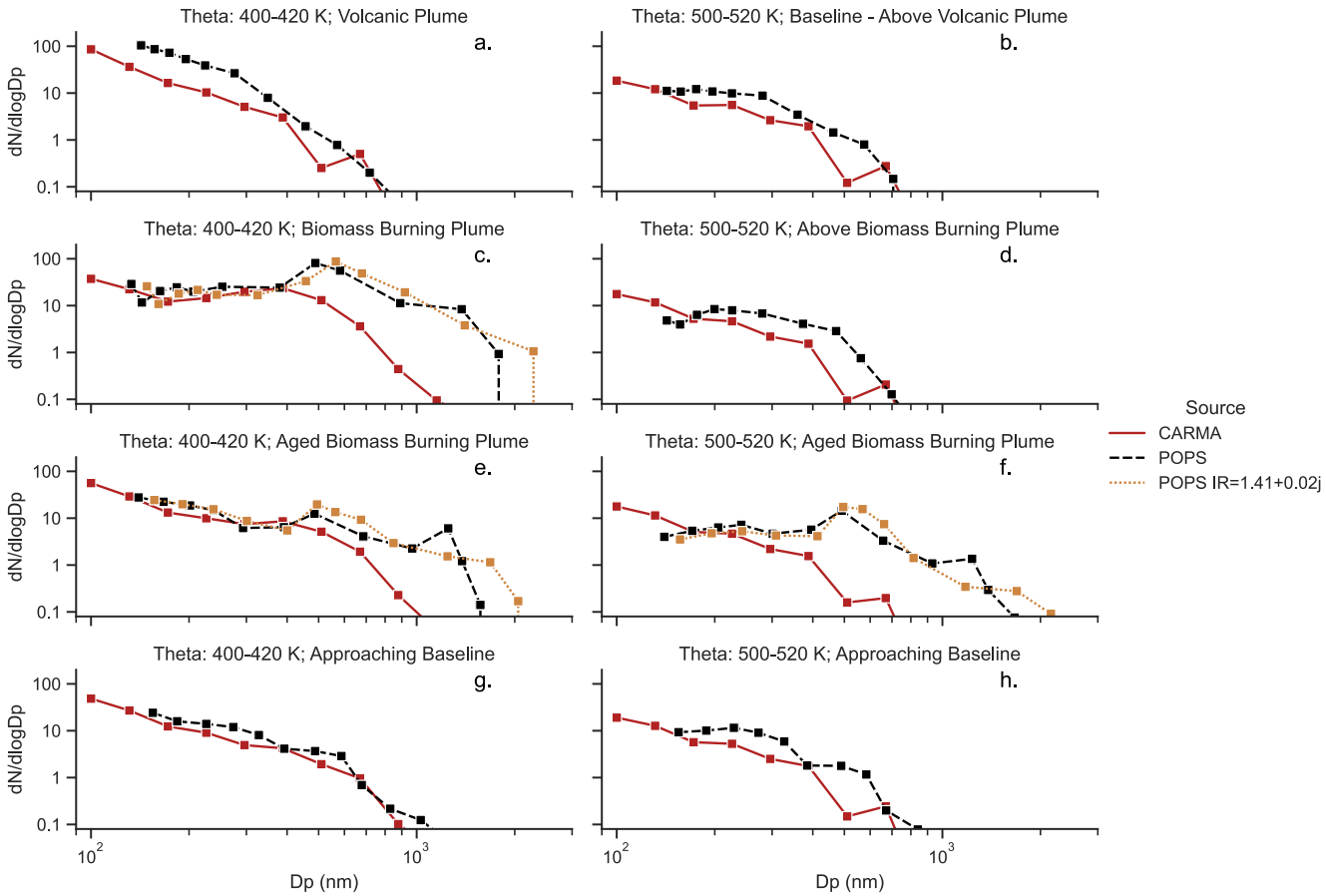

Figure 5. Ambient aerosol number concentration size distributions (normalized by bin width) from ascending flights, at two different isentropic levels (400–420 K and 500–520 K) from the POPS instrument and simulated by the CESM-CARMA model between 3 September 2019 (a–b) and 17 November 2020 (g–h). For reference, a POPS size distribution, assuming an alternative smoke IR = 1.41 + 0.02j at 405 nm is also shown for smoke cases (c, e, and f). Size distributions in air masses above the biomass burning plume (d) have noticeably fewer large particles.

stratosphere and sAOD with POPS total particle number concentration and sAOD calculated from both POPS size distributions and from lidar backscattering measurements. Simulated number concentration is lower than observed number concentration by a factor of ∼2 following the Ulawun volcanic eruption (Figure 7a), which is consistent with the model underestimating the number of small particles (≤300 nm in diameter) (Figure 5a), and to a lesser extent in other cases. Simulated sAOD ($\lambda = 521$ nm) agrees reasonably well with both POPS calculated and lidar-derived sAOD ($\lambda = 532$ nm). The difference in simulated and POPS calculated sAOD during this period is consistent with discrepancies in the number of large particles in the size distribution (>500–700 nm in diameter; Figures 5c, 5e and 5f) that have a proportionally greater impact on aerosol extinction (Murphy et al., 2021). We note that during this period, lidar-derived sAOD is also lower than POPS calculated sAOD (Figure 7b), in accordance with differences in extinction profiles between January 2020 and July 2020 (by factors of 1.4–1.6) (Figures 6c–6e).

In situ observations of aerosol microphysical properties reveal a balancing act between sedimentation, transport loss processes, evaporation, and new sources of stratospheric aerosol. As a result, particle number concentration and sAOD timeseries trends differ (Figure 7). POPS number concentration peaks after the Ulawun eruption in the SH tropics, and increases (slightly) again after the La Soufrière eruption in the NH tropics. According to both POPS and lidar measurements, the sAOD signal reaches a maximum after the ANYSO pyroCB and remains high for 6 months thereafter. This result suggests that changes in number concentration cannot be easily inferred from extinction measurements at a single wavelength. Recent work with SAGE III extinction profiles at multiple wavelengths shows promise for recovering information on stratospheric aerosol microphysics when dealing with a single-mode size distribution (Knepp et al., 2024).

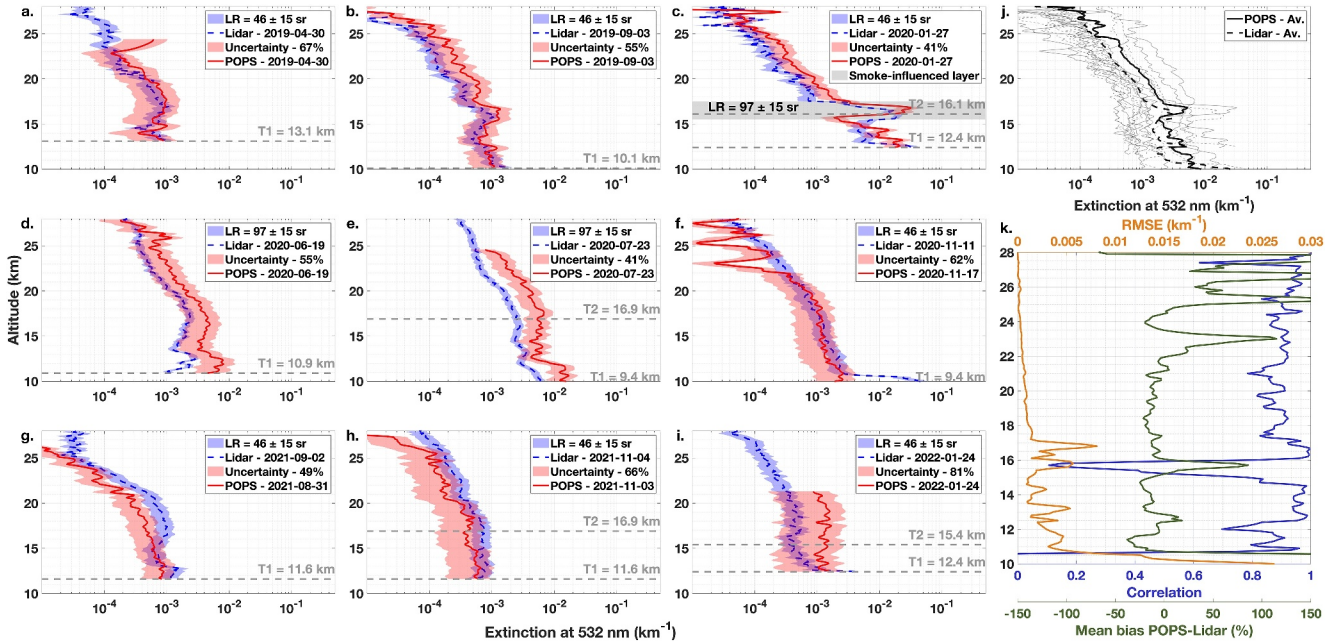

Figure 6. Ambient extinction profiles ($\lambda = 532$ nm) in the stratosphere from lidar and POPS. Panels (a–i) are POPS and lidar comparisons with the closest match in time from April 2019 to January 2022. The averages of both 9 profiles data set are plotted in (j) and statistics in k. (RMSE stands for root-mean-square error). Uncertainty in POPS extinction is calculated for each profile individually as a percentage, see an example of this calculation in Figure 1c insert. The individual profile extinction uncertainties are also listed in Table 1. Uncertainty in the lidar extinction is calculated based on ±15 sr in the lidar ratio.

4. Conclusions

B^{2}SAP soundings from Lauder, NZ provide insights into the magnitude and composition of stratospheric perturbations between 2019 and 2020 in SH midlatitudes and provide an important test for simulated size distributions from the CESM-CARMA model under baseline conditions as well as following injections of primary aerosol and aerosol precursors. The ANYSO pyroCB plume contained H_2O enhancements and had a large and prolonged impact on stratospheric aerosol size distributions (shifting the mode to a larger particle size diameter and resulting in a bimodal aerosol size distribution) over SH midlatitudes, which extended up into the middle stratosphere (Figures 4 and 5). Calculated aerosol extinction from balloon-based and ground-based instruments varied up to an order of magnitude after the ANYSO pyroCB, compared with baseline conditions in the stratosphere (Figures 6 and 7). Volcanic eruptions, such as Ulawun (5.05°S, 151.33°E) and La Soufrière (13.3°N, 61.2°W) likely caused observed increases in stratospheric number concentration (Figures 4 and 7). Our measurements reveal that CESM-CARMA lacks model skill in reproducing observations of aged BB airmass, indicating that more work must be done to fully understand the evolution of large pyroCB. In addition, comparisons of extinction calculated from POPS size distributions and from lidar backscattering measurements highlight a need for more measurements of aerosol composition and IR in fresh and aged biomass burning plumes.

One limitation for periodic balloon-borne in situ measurements is that it may be difficult to obtain a representative sample immediately after a perturbation. Intensive operations periods (IOP) targeting fresh volcanic (e.g., Asher et al., 2023) or pyroCB clouds with increased frequency, however, can be used to this shortcoming moving forward. Additionally, in situ measurements from a single location cannot provide insights into global impacts on climate and atmospheric chemistry related to large stratospheric perturbations. Extending the B^{2}SAP network to a range of other geographic regions, which began in 2022 with the addition of La Réunion Island, FR and Hilo, HI, will begin to address this weakness, supplementing the global coverage of satellite retrievals with more detailed information.

The SH midlatitudes remains an under sampled region in comparison with NH midlatitudes. Currently, more balloon-borne in situ aerosol size distribution measurements will be needed to quantify a baseline state for stratospheric aerosol microphysical properties in the SH, particularly below 17.5 km (450 K), given the short record and numerous perturbations reaching this altitude. Above 17.5 km median total aerosol number

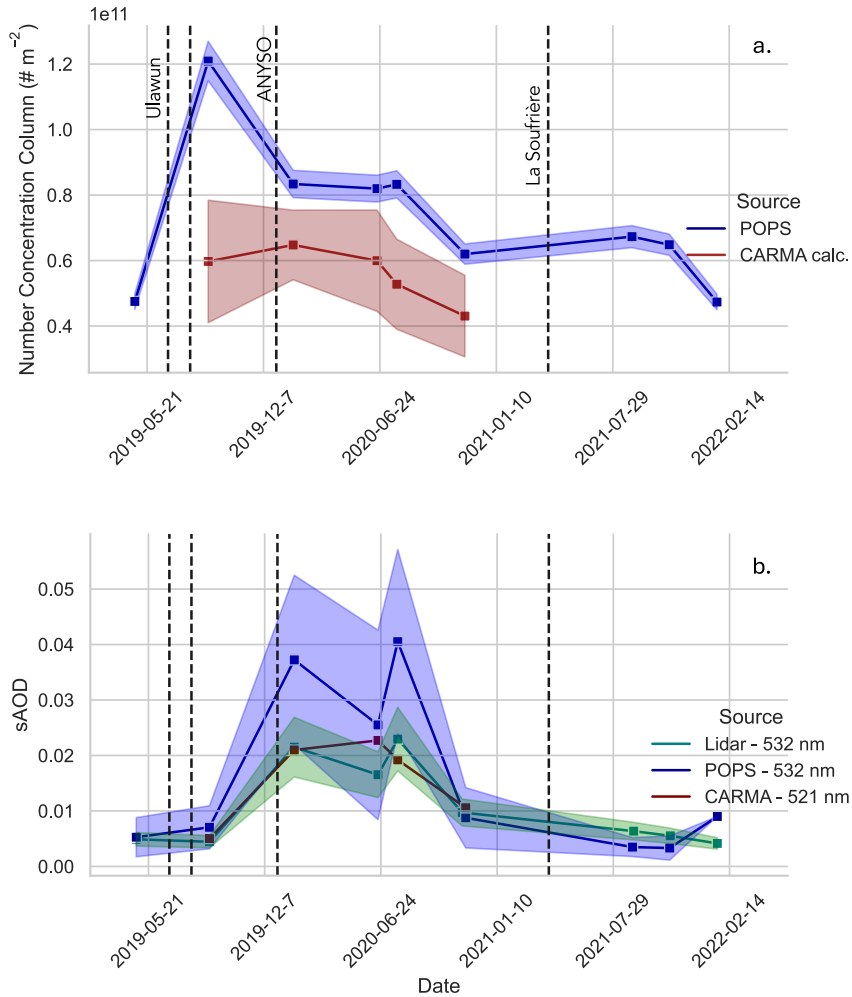

Figure 7. Available timeseries between 2019 and 2022 of observed and simulated total aerosol number concentration in the stratosphere (a) and sAOD (λ = 532 and 521 nm) (b) (potential temperature >380 K). POPS total particle concentration shows the 5% uncertainty related to the instrument flow. Due to differences in particle binning schemes, CARMA total number concentration shows the particle number <150 nm ± the range of particles between 115 and 198 nm in diameter. As noted elsewhere, POPS sAOD is calculated from measured aerosol size distributions and its uncertainty is based on sizing related to the aerosol composition (and IR). Lidar sAOD uncertainty of 25% is also shown. Dashed vertical lines indicate dates of stratospheric perturbations.

concentration in the SH midlatitudes decrease at a rate of ~0.6 cm^{-3} km^{-1} (in close agreement with baseline median values from NH midlatitudes; number concentration and surface area at S.T.P. are nearly constant with altitude; Figure 2). In both hemispheres, the maximum particle effective radius (~185 nm) occurs at 19 km altitude during this period. In combination with other sulfur cycle measurements, measurements of aerosol microphysical and optical properties in various geographic regions will be critical for understanding the natural variability in stratospheric aerosol and its impact on climate and for closing the sulfur budget.

Data Availability Statement

The quality assured and processed POPS size distribution data may be found under the supporting data tab for this manuscript at https://csl.noaa.gov/projects/b2sap/data.html (Asher, 2023) where processed lidar data, ozone and water vapor data, and output from CESM-CARMA simulations are also available. Code is publicly available (Asher, 2024).

Acknowledgments
This research was supported by the NOAA cooperative agreement NA22OAR4320151, the Earth Radiation Budget (ERB) project, and the NASA Upper Atmosphere Composition Observations (UACO) program. Lidar observation at Lauder is funded in part by the GOSAT (Greenhouse gases Observing SATellite) series project.

References

Aldhaif, A. M., Stahl, C., Braun, R. A., Moghaddam, M. A., Shingler, T., Crosbie, E., et al. (2018). Characterization of the real part of dry aerosol refractive index over North America from the surface to 12 km. *Journal of Geophysical Research: Atmospheres*, *123*(15), 8283–8300. https://doi.org/10.1029/2018JD028504

Allen, D. R., Fromm, M. D., Kablick Iii, G. P., & Nedoluha, G. E. (2020). Smoke with induced rotation and lofting (SWIRL) in the stratosphere. *Journal of the Atmospheric Sciences*, *77*(12), 4297–4316. https://doi.org/10.1175/JAS-D-20-0131.1

Andrews, D. G., Holton, J. R., & Leovy, C. B. (1987). *Middle atmosphere dynamics* (Vol. 40). Academic Press.

Asher, E. (2023). 2022-Asher-etal [Dataset]. Retrieved from https://csl.noaa.gov/groups/csl6/measurements/data/2022-Asher-etal/

Asher, E. (2024). elizabethasher/B2SAP_SH_19_22: Code for B2SAP - Perturbations in the Southern Hemisphere, 2019-2022 (Version v1.0). *Zenodo*. https://doi.org/10.5281/ZENODO.13963795

Asher, E., Todt, M., Rosenlof, K., Thornberry, T., Gao, R.-S., Taha, G., et al. (2023). Unexpectedly rapid aerosol formation in the Hunga Tonga plume. *Proceedings of the National Academy of Sciences*, *120*(46), e2219547120. https://doi.org/10.1073/pnas.2219547120

Bègue, N., Vignelles, D., Berthet, G., Portafaix, T., Payen, G., Jégou, F., et al. (2017). Long-range transport of stratospheric aerosols in the Southern Hemisphere following the 2015 Calbuco eruption. *Atmospheric Chemistry and Physics*, *17*(24), 15019–15036. https://doi.org/10.5194/acp-17-15019-2017

Bohren, C. F., & Huffman, D. R. (1983). *Absorption and scattering of light by small particles*. John Wiley and Sons.

Bruckert, J., Hirsch, L., Horváth, Á., Kahn, R. A., Kölling, T., Muser, L. O., et al. (2023). Dispersion and aging of volcanic aerosols after the La Soufrière eruption in April 2021. *Journal of Geophysical Research: Atmospheres*, *128*(8), e2022JD037694. https://doi.org/10.1029/2022JD037694

Burkholder, J. B., Sander, S. P., Abbatt, J. P. D., & Barker, J. R. (2015). Chemical kinetics and photochemical data for use in atmospheric studies: Evaluation number 18. *JPL Publication*, *15*(10)

Damany-Pearce, L., Johnson, B., Wells, A., Osborne, M., Allan, J., Belcher, C., et al. (2022). Australian wildfires cause the largest stratospheric warming since Pinatubo and extends the lifetime of the Antarctic ozone hole. *Scientific Reports*, *12*(1), 12665. https://doi.org/10.1038/s41598-022-15794-3

De Gouw, J. A., & Lovejoy, E. R. (1998). Reactive uptake of ozone by liquid organic compounds. *Geophysical Research Letters*, *25*(6), 931–934. https://doi.org/10.1029/98GL00515

Deshler, T., Hervig, M. E., Hofmann, D. J., Rosen, J. M., & Liley, J. B. (2003). Thirty years of in situ stratospheric aerosol size distribution measurements from Laramie, Wyoming (41°N), using balloon-borne instruments. *Journal of Geophysical Research*, *108*(D5), 2002JD002514. https://doi.org/10.1029/2002JD002514

Deshler, T., Luo, B., Kovilakam, M., Peter, T., & Kalnajs, L. E. (2019). Retrieval of aerosol size distributions from in situ particle counter measurements: Instrument counting efficiency and comparisons with satellite measurements. *Journal of Geophysical Research: Atmospheres*, *124*(9), 5058–5087. https://doi.org/10.1029/2018JD029558

Distributed by Smithsonian Institution, compiled by Venzke, E. (2023). Volcanoes of the world (v. 5.1.5; 15 Dec 2023) [Dataset]. *Global Volcanism Program*. https://doi.org/10.5479/si.GVP.VOTW5-2023.5.1

Forrister, H., Liu, J., Scheuer, E., Dibb, J., Ziemba, L., Thornhill, K. L., et al. (2015). Evolution of brown carbon in wildfire plumes. *Geophysical Research Letters*, *42*(11), 4623–4630. https://doi.org/10.1002/2015GL063897

Fromm, M., Lindsey, D. T., Servranckx, R., Yue, G., Trickl, T., Sica, R., et al. (2010). The untold story of pyrocumulonimbus. *Bulletin of the American Meteorological Society*, *91*(9), 1193–1210. https://doi.org/10.1175/2010BAMS3004.1

Froyd, K. D., Murphy, D. M., Sanford, T. J., Thomson, D. S., Wilson, J. C., Pfister, L., & Lait, L. (2009). Aerosol composition of the tropical upper troposphere. *Atmospheric Chemistry and Physics*, *9*(13), 4363–4385. https://doi.org/10.5194/acp-9-4363-2009

Gao, R. S., Perring, A. E., Thornberry, T. D., Rollins, A. W., Schwarz, J. P., Ciciora, S. J., & Fahey, D. W. (2013). A high-sensitivity low-cost optical particle counter design. *Aerosol Science and Technology*, *47*(2), 137–145. https://doi.org/10.1080/02786826.2012.733039

Gao, R. S., Telg, H., McLaughlin, R. J., Ciciora, S. J., Watts, L. A., Richardson, M. S., et al. (2016). A light-weight, high-sensitivity particle spectrometer for PM2.5 aerosol measurements. *Aerosol Science and Technology*, *50*(1), 88–99. https://doi.org/10.1080/02786826.2015.1131809

Global Volcanism Program. (2019). Report on Ulawun (Papua New Guinea). In E. Venzke ed. *Bulletin of the Global Volcanism Network*, (Vol. 44, pp. 9). Smithsonian Institution. https://doi.org/10.5479/si.GVP.BGVN201909-252120

Gmitro, J. I., & Vermeulen, T. (1964). Vapor-liquid equilibria for aqueous sulfuric acid. *AIChE Journal*, *10*(5), 740–746. https://doi.org/10.1002/aic.690100531

Hall, E. G., Jordan, A. F., Hurst, D. F., Oltmans, S. J., Vömel, H., Kühnreich, B., & Ebert, V. (2016). Advancements, measurement uncertainties, and recent comparisons of the NOAAfrost point hygrometer. *Atmospheric Measurement Techniques*, *9*(9), 4295–4310. https://doi.org/10.5194/amt-9-4295-2016

Hitchman, M. H., McKay, M., & Trepte, C. R. (1994). A climatology of stratospheric aerosol. *Journal of Geophysical Research*, *99*(D10), 20689. https://doi.org/10.1029/94JD01525

Hurst, D. F., Oltmans, S. J., Vömel, H., Rosenlof, K. H., Davis, S. M., Ray, E. A., et al. (2011). Stratospheric water vapor trends over Boulder, Colorado: Analysis of the 30 year Boulder record. *Journal of Geophysical Research*, *116*(D2), D02306. https://doi.org/10.1029/2010JD015065

Intergovernmental Panel On Climate Change (IPCC). (2023). *Climate change 2021 – the physical science basis: Working group I contribution to the sixth assessment report of the intergovernmental panel on climate change* (1st ed.). Cambridge University Press. https://doi.org/10.1017/9781009157896

Junge, C. E., & Manson, J. E. (1961). Stratospheric aerosol studies. *Journal of Geophysical Research*, *66*(7), 2163–2182. https://doi.org/10.1029/JZ066i007p02163

Kablick, G. P., Allen, D. R., Fromm, M. D., & Nedoluha, G. E. (2020). Australian PyroCb smoke generates synoptic-scale stratospheric anticyclones. *Geophysical Research Letters*, *47*(13), e2020GL088101. https://doi.org/10.1029/2020GL088101

Katich, J. M., Apel, E. C., Bourgeois, I., Brock, C. A., Bui, T. P., Campuzano-Jost, P., et al. (2023). Pyrocumulonimbus affect average stratospheric aerosol composition. *Science*, *379*(6634), 815–820. https://doi.org/10.1126/science.add3101

Khaykin, S., Legras, B., Bucci, S., Sellitto, P., Isaksen, L., Tencé, F., et al. (2020). The 2019/20 Australian wildfires generated a persistent smoke-charged vortex rising up to 35 km altitude. *Communications Earth & Environment*, *1*(1), 22. https://doi.org/10.1038/s43247-020-00022-5

Kirchstetter, T. W., Novakov, T., & Hobbs, P. V. (2004). Evidence that the spectral dependence of light absorption by aerosols is affected by organic carbon. *Journal of Geophysical Research*, *109*(D21), 2004JD004999. https://doi.org/10.1029/2004JD004999

Kloss, C., Berthet, G., Sellitto, P., Ploeger, F., Taha, G., Tidiga, M., et al. (2021). Stratospheric aerosol layer perturbation caused by the 2019 Raikoke and Ulawun eruptions and their radiative forcing. *Atmospheric Chemistry and Physics*, *21*(1), 535–560. https://doi.org/10.5194/acp-21-535-2021

Knepp, T. N., Kovilakam, M., Thomason, L., & Miller, S. J. (2024). Characterization of stratospheric particle size distribution uncertainties using SAGE II and SAGE III/ISS extinction spectra. *Atmospheric Measurement Techniques*, *17*(7), 2025–2054. https://doi.org/10.5194/amt-17-2025-2024

Komhyr, W. D., & Harris, T. B. (1971). *Development of an ECC ozonesonde* (Vol. 54). Atmosheric Physics and Chemistry Laboratory.

Kovilakam, M., & Deshler, T. (2015). On the accuracy of stratospheric aerosol extinction derived from in situ size distribution measurements and surface area density derived from remote SAGE II and HALOE extinction measurements. *Journal of Geophysical Research: Atmospheres*, *120*(16), 8426–8447. https://doi.org/10.1002/2015JD023303

Kräuchi, A., Philipona, R., Romanens, G., Hurst, D. F., Hall, E. G., & Jordan, A. F. (2016). Controlled weather balloon ascents and descents for atmospheric research and climate monitoring. *Atmospheric Measurement Techniques*, *9*(3), 929–938. https://doi.org/10.5194/amt-9-929-2016

Kremser, S., Thomason, L. W., Von Hobe, M., Hermann, M., Deshler, T., Timmreck, C., et al. (2016). Stratospheric aerosol-Observations, processes, and impact on climate: Stratospheric Aerosol. *Reviews of Geophysics*, *54*(2), 278–335. https://doi.org/10.1002/2015RG000511

Mackowski, D. W., & Mishchenko, M. I. (2011). A multiple sphere T-matrix Fortran code for use on parallel computer clusters. *Journal of Quantitative Spectroscopy and Radiative Transfer*, *112*(13), 2182–2192. https://doi.org/10.1016/j.jqsrt.2011.02.019

Murphy, D. M., Abou-Ghanem, M., Cziczo, D. J., Froyd, K. D., Jacquot, J., Lawler, M. J., et al. (2023). Metals from spacecraft reentry in stratospheric aerosol particles. *Proceedings of the National Academy of Sciences*, *120*(43), e2313374120. https://doi.org/10.1073/pnas.2313374120

Murphy, D. M., Froyd, K. D., Bourgeois, I., Brock, C. A., Kupc, A., Peischl, J., et al. (2021). Radiative and chemical implications of the size and composition of aerosol particles in the existing or modified global stratosphere. *Atmospheric Chemistry and Physics*, *21*(11), 8915–8932. https://doi.org/10.5194/acp-21-8915-2021

Murphy, D. M., Froyd, K. D., Schwarz, J. P., & Wilson, J. C. (2014). Observations of the chemical composition of stratospheric aerosol particles. *Quarterly Journal of the Royal Meteorological Society*, *140*(681), 1269–1278. https://doi.org/10.1002/qj.2213

Novak, G. A., Fite, C. H., Holmes, C. D., Veres, P. R., Neuman, J. A., Faloona, I., et al. (2021). Rapid cloud removal of dimethyl sulfide oxidation products limits SO_2 and cloud condensation nuclei production in the marine atmosphere. *Proceedings of the National Academy of Sciences*, *118*(42), e2110472118. https://doi.org/10.1073/pnas.2110472118

Oca, L., Campillo-Robles, J. M., & Bou-Ali, M. M. (2018). Review and analysis of thermophysical properties of a sulfuric acid–water electrolyte. *Journal of Chemical and Engineering Data*, *63*(9), 3572–3583. https://doi.org/10.1021/acs.jced.8b00466

Ohneiser, K., Ansmann, A., Baars, H., Seifert, P., Barja, B., Jimenez, C., et al. (2020). Smoke of extreme Australian bushfires observed in the stratosphere over Punta Arenas, Chile, in January 2020: Optical thickness, lidar ratios, and depolarization ratios at 355 and 532 nm. *Atmospheric Chemistry and Physics*, *20*(13), 8003–8015. https://doi.org/10.5194/acp-20-8003-2020

Ohneiser, K., Ansmann, A., Kaifler, B., Chudnovsky, A., Barja, B., Knopf, D. A., et al. (2022). Australian wildfire smoke in the stratosphere: The decay phase in 2020/2021 and impact on ozone depletion. *Atmospheric Chemistry and Physics*, *22*(11), 7417–7442. https://doi.org/10.5194/acp-22-7417-2022

Peterson, D. A., Campbell, J. R., Hyer, E. J., Fromm, M. D., Kablick, G. P., Cossuth, J. H., & DeLand, M. T. (2018). Wildfire-driven thunderstorms cause a volcano-like stratospheric injection of smoke. *Npj Climate and Atmospheric Science*, *1*(1), 30. https://doi.org/10.1038/s41612-018-0039-3

Peterson, D. A., Fromm, M. D., McRae, R. H. D., Campbell, J. R., Hyer, E. J., Taha, G., et al. (2021). Australia's Black Summer pyrocumulonimbus super outbreak reveals potential for increasingly extreme stratospheric smoke events. *Npj Climate and Atmospheric Science*, *4*(1), 38. https://doi.org/10.1038/s41612-021-00192-9

Petters, M. D., & Kreidenweis, S. M. (2007). A single parameter representation of hygroscopic growth and cloud condensation nucleus activity. *Atmospheric Chemistry and Physics*, *7*(8), 1961–1971. https://doi.org/10.5194/acp-7-1961-2007

Prata, A. T., Young, S. A., Siems, S. T., & Manton, M. J. (2017). Lidar ratios of stratospheric volcanic ash and sulfate aerosols retrieved from CALIOP measurements. *Atmospheric Chemistry and Physics*, *17*(13), 8599–8618. https://doi.org/10.5194/acp-17-8599-2017

Pumphrey, H. C., Santee, M. L., Livesey, N. J., Schwartz, M. J., & Read, W. G. (2011). Microwave Limb Sounder observations of biomass-burning products from the Australian bush fires of February 2009. *Atmospheric Chemistry and Physics*, *11*(13), 6285–6296. https://doi.org/10.5194/acp-11-6285-2011

Rollins, A. W., Thornberry, T. D., Atlas, E., Navarro, M., Schauffler, S., Moore, F., et al. (2018). SO_2 observations and sources in the Western Pacific tropical tropopause region. *Journal of Geophysical Research: Atmospheres*, *123*(23), 13–549. https://doi.org/10.1029/2018JD029635

Rollins, A. W., Thornberry, T. D., Watts, L. A., Yu, P., Rosenlof, K. H., Mills, M., et al. (2017). The role of sulfur dioxide in stratospheric aerosol formation evaluated by using in situ measurements in the tropical lower stratosphere. *Geophysical Research Letters*, *44*(9), 4280–4286. https://doi.org/10.1002/2017GL072754

Sakai, T., Uchino, O., Nagai, T., Liley, B., Morino, I., & Fujimoto, T. (2016). Long-term variation of stratospheric aerosols observed with lidars over Tsukuba, Japan, from 1982 and Lauder, New Zealand, from 1992 to 2015: LIDAR-OBSERVED stratospheric aerosols. *Journal of Geophysical Research: Atmospheres*, *121*(17), 10283–10293. https://doi.org/10.1002/2016JD025132

Schwartz, M. J., Santee, M. L., Pumphrey, H. C., Manney, G. L., Lambert, A., Livesey, N. J., et al. (2020). Australian New Year's PyroCb impact on stratospheric composition. *Geophysical Research Letters*, *47*(24), e2020GL090831. https://doi.org/10.1029/2020GL090831

Shamjad, P. M., Tripathi, S. N., Aggarwal, S. G., Mishra, S. K., Joshi, M., Khan, A., et al. (2012). Comparison of experimental and modeled absorption enhancement by black carbon (BC) cored polydisperse aerosols under hygroscopic conditions. *Environmental Science & Technology*, *46*(15), 8082–8089. https://doi.org/10.1021/es300295v

Solomon, S., Daniel, J. S., Neely, R. R., Vernier, J.-P., Dutton, E. G., & Thomason, L. W. (2011). The persistently variable "background" stratospheric aerosol layer and global climate change. *Science*, *333*(6044), 866–870. https://doi.org/10.1126/science.1206027

Sumlin, B. J., Heinson, W. R., & Chakrabarty, R. K. (2018). Retrieving the aerosol complex refractive index using PyMieScatt: A Mie computational package with visualization capabilities. *Journal of Quantitative Spectroscopy and Radiative Transfer*, *205*, 127–134. https://doi.org/10.1016/j.jqsrt.2017.10.012

Tabazadeh, A., Toon, O. B., Clegg, S. L., & Hamill, P. (1997). A new parameterization of H_2SO_4/H_2O aerosol composition: Atmospheric implications. *Geophysical Research Letters*, *24*(15), 1931–1934. https://doi.org/10.1029/97GL01879

Tilmes, S., Richter, J. H., Mills, M. J., Kravitz, B., MacMartin, D. G., Vitt, F., et al. (2017). Sensitivity of aerosol distribution and climate response to stratospheric SO_2 injection locations. *Journal of Geophysical Research: Atmospheres*, *122*(23), 12–591. https://doi.org/10.1002/2017JD026888

Todt, M. A., Asher, E., Hall, E., Cullis, P., Jordan, A., Xiong, K., et al. (2023). Baseline balloon stratospheric aerosol profiles (B ^{2} SAP)—Systematic measurements of aerosol number density and size. *Journal of Geophysical Research: Atmospheres*, *128*(12), e2022JD038041. https://doi.org/10.1029/2022JD038041

Veres, P. R., Neuman, J. A., Bertram, T. H., Assaf, E., Wolfe, G. M., Williamson, C. J., et al. (2020). Global airborne sampling reveals a previously unobserved dimethyl sulfide oxidation mechanism in the marine atmosphere. *Proceedings of the National Academy of Sciences*, *117*(9), 4505–4510. https://doi.org/10.1073/pnas.1919344117

Washburn, E. W. (Ed.) (1928)., *International critical tables of numerical data, physics, chemistry and technology* (Vol. III). McGraw-Hill.

Williamson, C. J., Kupc, A., Axisa, D., Bilsback, K. R., Bui, T., Campuzano-Jost, P., et al. (2019). A large source of cloud condensation nuclei from new particle formation in the tropics. *Nature*, *574*(7778), 399–403. https://doi.org/10.1038/s41586-019-1638-9

Yu, P., Davis, S. M., Toon, O. B., Portmann, R. W., Bardeen, C. G., Barnes, J. E., et al. (2021). Persistent stratospheric warming due to 2019–2020 Australian wildfire smoke. *Geophysical Research Letters*, *48*(7), e2021GL092609. https://doi.org/10.1029/2021GL092609

Yu, P., Portmann, R. W., Peng, Y., Liu, C., Zhu, Y., Asher, E., et al. (2023). Radiative forcing from the 2014–2022 volcanic and wildfire injections. *Geophysical Research Letters*, *50*(13), e2023GL103791. https://doi.org/10.1029/2023GL103791

Yu, P., Toon, O. B., Bardeen, C. G., Mills, M. J., Fan, T., English, J. M., & Neely, R. R. (2015). Evaluations of tropospheric aerosol properties simulated by the community earth system model with a sectional aerosol microphysics scheme. *Journal of Advances in Modeling Earth Systems*, *7*(2), 865–914. https://doi.org/10.1002/2014MS000421

Yu, P., Toon, O. B., Bardeen, C. G., Zhu, Y., Rosenlof, K. H., Portmann, R. W., et al. (2019). Black carbon lofts wildfire smoke high into the stratosphere to form a persistent plume. *Science*, *365*(6453), 587–590. https://doi.org/10.1126/science.aax1748

Zhu, Y., Toon, O. B., Jensen, E. J., Bardeen, C. G., Mills, M. J., Tolbert, M. A., et al. (2020). Persisting volcanic ash particles impact stratospheric SO2 lifetime and aerosol optical properties. *Nature Communications*, *11*(1), 4526. https://doi.org/10.1038/s41467-020-18352-5